A Study of Hydrogen Recombination Masers in MWC349A

Brian W. Claus[1]
Advisors: Dr. Qizhou Zhang[1], Dr. Linda Watson[1]
[1]Harvard-Smithsonian Center for Astrophysics

Abstract

Using the Submillimeter Array we performed subarcsecond resolution observations of H26α and H30α recombination lines in MWC349A in order to map the distribution of this emission as many distinct maser spots. The high signal-to-noise ratio of the maser emission allows us to constrain the position of the maser spots to milliarcsecond precision at a maximum velocity resolution of 0.53 km/s. We confirm previous observations showing that the majority of the maser spots are located in a strip thought to trace out the disk of gas surrounding the star. We then use this data to compare the positions of H26α and H30α maser spots and to analyze the structure of the disk of gas around MWC349A.

1. Introduction

MWC349A is one star of a binary pair located 1.2 kiloparsecs from earth in the constellation Cygnus. The system is classified as a B[e] system indicating that both stars are B type stars and that hydrogen emission features are observed in the system. The source of this emission has been traced to maser emission occurring in a circumstellar disk of gas surrounding MWC349A (Martin-Pintado et al. 1989). Maser is an acronym for Microwave Amplification of Stimulated Emission of Radiation. The commonly accepted explanation for this maser emission is that it is occurring in an ionized disk of gas surrounding MWC349A (Thum et al. 1994a,b). The origin of this gas is unknown; it could be part of a protoplanetary system, gas that MWC349A has accreted from its neighbor MWC349B, or gas that it has shed from its own envelope. As hydrogen atoms in this disk undergo recombination they release a photon of the associated Balmer wavelength. This photon stimulates other hydrogen atoms to release photons of the same wavelength, phase, and direction of propagation. Those photons in turn can stimulate additional hydrogen atoms. This process quickly leads to a coherent beam of photons that all

travel together without destructive interference producing an extremely bright signal. Maser emission around stars like this is a rare phenomenon.

The initial discover noted 4 hydrogen emission features: H29α, H30α, H31α, and H41α (Martin-Pintado et al. 1989). These refer to the different Balmer emission lines associated with electron transitions in the hydrogen atoms. Subsequent studies have discovered many additional Balmer emission lines that are thought to be a result of different frequency maser emission in the disk around MWC349a.

Previous studies have shown that the maser emission around MWC349A is located in a collection of discrete locations around the disk referred to as "maser spots" (Weintroub et al, 2008). The process for the formation of these maser spots is still unknown. Previous studies have managed to measure the position of H30α maser spots to a precision of 0.01 arcseconds at a velocity resolution of 1 km/s (Weintroub et al, 2008). We present data improving on these results. We have improved the positional accuracy of H30α maser spots down to milliarcsecond precision and have also increased the velocity resolution to 0.53 km/s. We have also performed similar observations of the H26α maser spots. We hope that by further constraining maser spot positions we can produce a more detailed model of the disk's shape. In addition we plan to compare the positions of the H30α and H26α maser spots to investigate the source of this maser phenomenon. In this paper we will cover the procedure we used to take our observations, the steps we used to calibrate our data, present comparisons of the H26α and H30α data. We will include some preliminary analysis of disk structure but detailed analysis of the disk structure will be left for a later paper.

2. Observations

2.1 Instrument

The instrument we used for our observation was the Submillimeter Array (SMA) located atop Mauna Kea in Hawaii at an elevation of 4080 meters. The SMA is an interferometer consisting of 8 6-meter telescopes that can be configured in 4 different configurations: subcompact (baselines of 9.5-70 m), compact (baselines of 16.5-70 m), extended (baselines up to 220 m), and very-extended (baselines up to 500 m). (Ho et al. 2004) Since our goals call for the highest possible angular resolution we chose to observe when the SMA was in the very-extended configuration. More extended configurations do come with the drawback of reducing our sensitivity to the surface brightness distribution of our source. However our object is not spatially resolved even with the very-extended configuration of the SMA and therefore we do not have a surface brightness distribution to worry about anyways.

2.2 Choice of Observing Frequencies

We chose to observe two hydrogen emission lines: the H30α line (231 GHz) and H26α (353.6 GHz). We choose these lines in order to maximize the received signal. Higher frequency lines usually produce brighter emission lines in astrophysical masers but higher frequencies are also absorbed more strongly by the earth's atmosphere. H30α is a good compromise between these two competing effects. We observed H26α as well in order to take advantage of a particular feature of the SMA telescopes: they can each be loaded with 2 receivers during a single observation. However the actual mechanical setup of the antenna limits which receivers we can pair together so we were limited in which second frequency we could observe. We choose to observe H26α first of all since it was technically possible with the dual receive setup, and also because it also was a good compromise between the competing effects of maser brightness and atmospheric absorption. The H26α maser emission is significantly brighter than the H30α emission but the H26α emission is absorbed significantly more by the atmosphere than H30α.

The increased effect of the atmosphere made the H26α data much more difficult to calibrate. We'll discuss the specifics of this calibration in the next section.

2.3 Observing

Our observations were carried out October 12th 3:16:35 – 17:21:19 UT. We did not carry out the actual observations; we submitted an observing script that was approved and then carried out by observers at the SMA site in Mauna Kea. For our observations only 6 of the SMA telescopes were operational (antennas 1,2,3,5,6,7,). This reduced our overall signal strength but not so much as to compromise our data. The humidity at Mauna Kea increased dramatically towards the end of our experiment. From 12 UT onwards the heightened humidity drastically increased the noise in our measurements. We were still able to salvage almost all of the data from this period. A lot of time went into calibrating our data to overcome the effects of this bad weather.

We also observed several calibrator objects during our observation period. We observed the quasar 2015+371 for use as a gain calibrator, Calisto as a flux calibrator (although we ultimately did not use it), and the quasar 3C84 as a bandpass calibrator. The observations of 3C84 were unique since we used an unusual method to improve our bandpass calibration. We discuss this further in the later section of this paper covering data calibration.

3. Data Reduction

3.1 Data Calibration

Our raw data consisted of the correlator output from each set of antennas. These data are referred to as a Visibility Function.

$$V(u,v) = FT [\ I(l,m)\ ]$$

This visibility function gives an amplitude and phase value for each 2-dimensional baseline represented by its two components: u and v. The amplitude of this visibility function signifies how much emission is coming from a certain position while the phase signifies where that emission lies on a positional map. l and m in the above equation refers to Ra and Dec respectively, the two coordinates on the sky. Before we can create an image we first need to calibrate our visibility function by removing several sources of systematic error. We performed the following set of calibrations using the MIR software package. Unless otherwise noted these calibrations were performed in the same way for the H26α and H30α data.

The first correction we applied was our system temperature correction. Our observations were taken over a very long time period and over time our target object's position in the sky changes significantly. When our object is close to rising or setting we are observing through a much higher amount of atmosphere than when our object is close to zenith. Our data contained the elevation of each antenna at every point in time as well as a record of the corresponding system temperature. For each baseline we plotted elevation against system temperature and examined the resulting curves. Since our object moves smoothly across the sky, we expect these curves to be smooth functions with no discontinuities. We removed any outlier discontinuous points, and then use a built in MIR command to apply each calibration to the appropriate baseline to obtain the appropriate flux. Looking through more atmosphere reduces the intensity of a signal so this calibration corrects for that effect by scaling the measured flux by the amount of atmosphere that antenna was looking through.

Next we need to make a bandpass correction: correcting for our receiver's differential response to a range of frequencies. To do this we observe an object that has no spectral features; in our experiment we observed the quasar 3C84. Since this object has no spectral features our

receiver should respond equally to it across all wavelengths. Instead of that expected response we observe a particular response that characterizes our receiver's response to different frequencies. Most of this response is caused by our telescope's filter; frequencies towards the center of the filter's spectral range are much less attenuated than frequencies towards the edges of its spectral range. We then use the offset between this observation and the flat spectra we expect from our calibrator to remove this systematic effect from the rest of our data. For the H26α data we used a trick to obtain a more accurate bandpass calibration solution. The 353 GHz signal from 3C84 was much weaker than our 230 GHz signal so while taking our observations we actually passed the 230 GHz signal of 3C84 through the electronics system of the 353 GHz receiver. This will still yield a correct bandpass solution as long as the majority of the source of the error the bandpass calibration corrects for is due to the receiver's electronics system rather than any atmospheric effect. We are confident that the atmospheric effect is minimal compared to the effects caused by the instrumental electronics, particularly the filter of the receiver. However we still need to examine whether the difference is large enough to affect our final data and this is a topic we will look into further as we proceed with this project. Employing this tactic allowed us to obtain a much better bandpass calibration than we would have had for the H26α data since we were able to use data with a much higher signal:noise to make this calibration.

It is important to note that errors in the bandpass calibration can introduce large errors in our maser spot positions. Since, as we will later explain, we are examining the maser emission at different frequencies, converting those to a velocity, and then finding the center of the emission at that velocity it is extremely important that we remove any frequency phase trend during the bandpass calibration stage. A failure to remove erroneous phase offsets would introduce erroneous position information into our dataset.

The following two steps, flux calibration and gain calibration, were only done for the H30α data. We did these corrections as part of our self-calibration for the H26α data. We need to scale our flux measurements by observing an object of known flux and scaling all our flux measurements to that object. We observed Calisto to use as a flux calibrator but unfortunately we carried out that observation towards the end of our observations, during the period in which the humidity was too high for us to get accurate data. We were able to use the continuum emission from our own object, MWC349a, as a flux calibrator since it is a very bright object of known flux. We then applied the solution for the continuum emission to calibrate our line data.

Finally we had to perform a gain calibration to remove atmospheric effects that changed over time. To do this we observed a point source, the quasar 2015+371, periodically while taking our data. Observing a point source with an interferometer should give you a visibility function of constant phase and amplitude. However atmospheric fluctuations cause our data to differ from an unaffected observation. By observing this quasar we can see how the atmospheric fluctuations are affecting the data and calibrate to remove those effects.

After doing these basis calibrations we applied a special self-calibration procedure that only works for bright sources that we already have a very good model for. For our beam size (31"x 36") MWC349A is a very bright point source. In interferometry points a source located at the center of the antennae view produces a correlator output of constant amplitude and 0 phase. We can use this is a model for the continuum emission of MWC349A and compare that to the continuum emission in our data set to produce a correction we can apply to the spectral line features. Ultimately these spectral line features are what we are interested in since they correspond to the maser spots.

To perform this calibration we separated the continuum emission data from the "line data:" the part of the dataset we believed contained maser emission. We then found a model for how the amplitude and phase of the continuum emission varied with time, and applied this correction to the line data. For H30α we only performed a calibration on the phase but on the H26α data we performed a calibration on the phase and the amplitude of the line data.

We also performed a second self-calibration step for the H26α data since it was more affected by the period of bad weather. For this calibration we took the brightest maser feature (31 km/s) and used its amplitude and phase over time to create a solution we could apply to the rest of the line data. This line self-calibration was much more successful than the continuum self-calibration because the signal:noise ratio was much higher for our brightest maser feature than it was for the dim continuum emission. However this calibration procedure did introduce a position shift into our dataset. By using the model for that brightest maser feature to calibrate our data we set its phase to 0, which made it the center of our resultant image. This introduces a ~0.02 arcsecond positional shift between the center of the H30α image and the center of the H26α image. In the future we will go back and redo the calibration to remove this shift. One way to remove the shift would be to perform the line self-calibration for the H30α data as well. Even with this position shift we are still able to easily compare our data for the 2 different maser features by simply shifting the H26α dataset ~0.02" to the left to align the 31 km/s feature in each dataset.

3.2 Imaging

After calibrating our data to remove the systematic errors we are left with our correct visibility as a function of baseline in two coordinates (u and v). To go from this visibility

function to our clean image we a series of commands in the MIRIAD software package that performed the mathematical calculations for us.

First we need to convert our visibility distribution into a sky brightness distribution using the following equation:

$$V(u,v) \ * \ S(u,v) = FT \ [\ I^{Dirty}(l,m) \ ]$$

$V(u,v)$ is the visibility function we observed, $I^{Dirty}(l,m)$ is the dirty image, and $S(u,v)$ is the sampling distribution, a function of all the 2 dimensional baselines configurations we had throughout our observing period. We need to take the inverse Fourier Transform of the visibility function convolved with the sampling distribution. The Convolution Theorem tells us that taking the Fourier Transform of convolved functions is the same as taking the Fourier transform of each and then convolving them. Carrying out this inverse Fourier Transform we get:

$$I^{Dirty}(l,m) = I(l,m) \ * \ S^{Dirty}(l,m)$$

$I(l,m)$ is the true sky brightness distribution and $S(l,m)$ is our dirty beam. Finally, we need to deconvolve the dirty beam from the dirty image to determine a model for the true sky brightness distribution. Our clean image is the convolution of this model sky brightness distribution with the clean beam (a Gaussian function that has the same FWHM as the dirty beam) plus the residual image (an image of the noise from our original data). For most of our analysis we chose to operate with the visibility data rather than the image. Working with the visibility is usually superior since some information in the image is incorrect information arising from the convolution with the imperfect clean beam.

4. Analysis

After imaging our data we are left with a series of images with one in each frequency channel. These images give us a measure of intensity as a function of position (Ra, Dec).
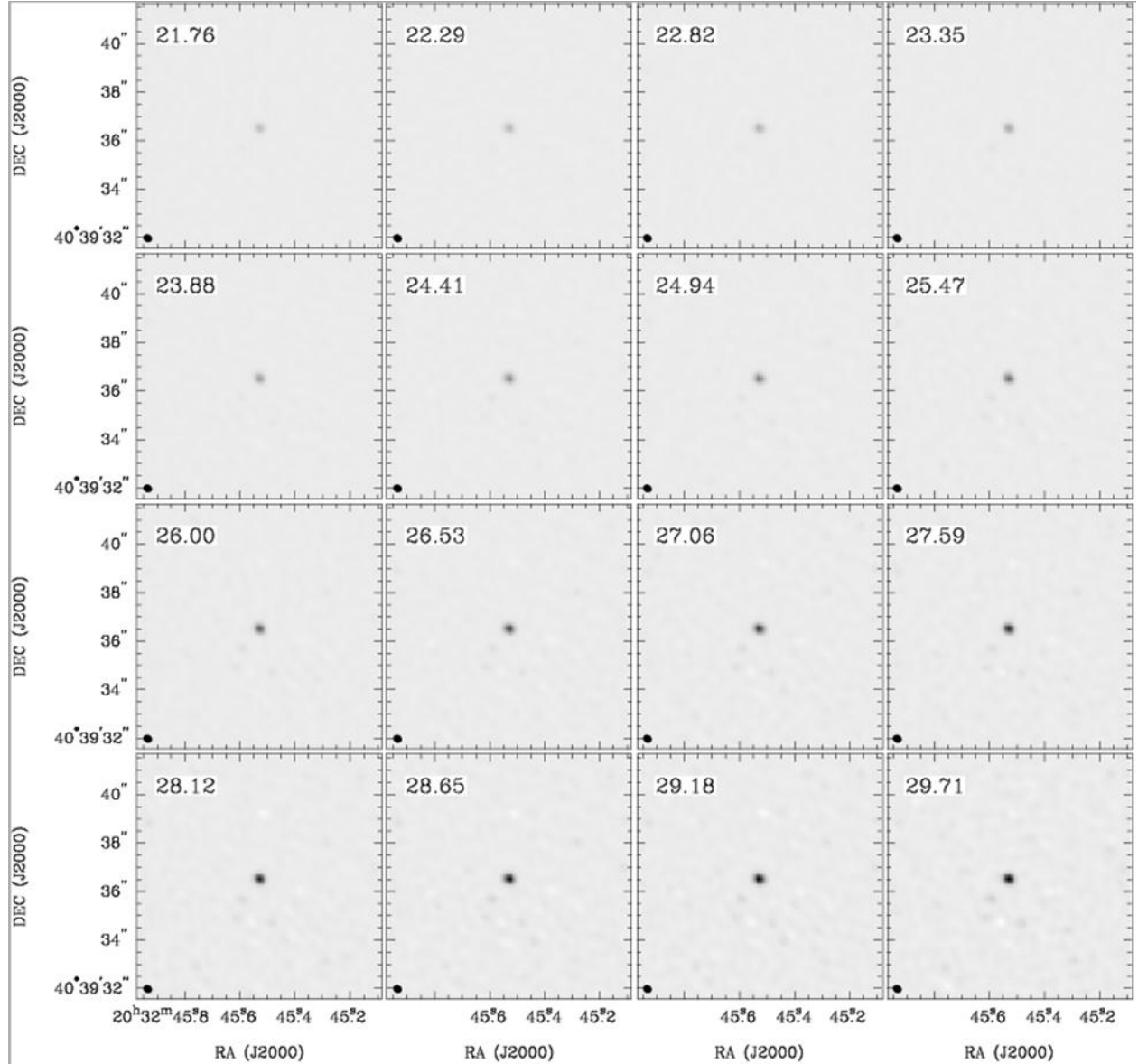
Figure 1: A monitor display showing 20 of these images for the H30α dataset. Each window is an image of the radiation at a particular frequency. Brightness corresponds to total intensity. RA is on the x axes and Declination is on the y axes for each image. RA is reported as hour angle, arcminutes, arcseconds, Declination as degrees, arcminutes, arcseconds, and velocity as km/s from the rest frequency of H30 α. The dot in the center of each image is MWC349a and the dot in the bottom left corner is a marker added to show the size of our synthesized beam (~0.31"x0.36"). Windows with a very faint central dot indicate very little maser emission at that frequency while windows with a well-defined dot indicate strong maser emission at that frequency. Note that the each window differs from the previous window by 0.53 km/s since that is our velocity resolution.

The total extent of MWC349a is less than our synthesized beam size so it is a point source in these images. Measuring all the flux in each velocity channel allows us to create an integrated line profile for MWC349a H30 α emission:
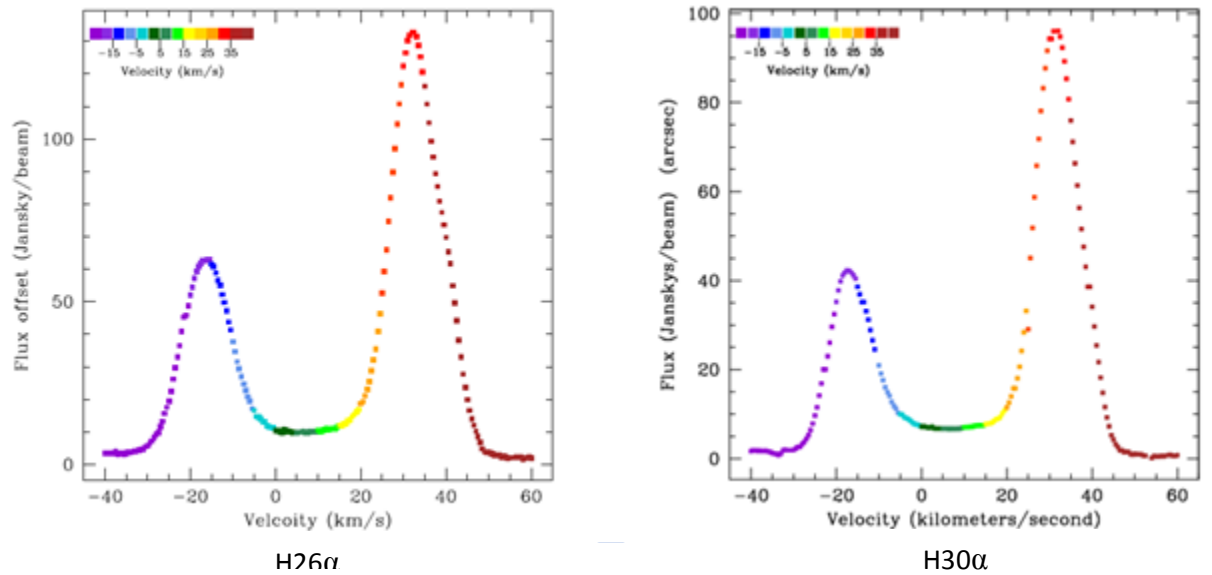

Figure 2: Integrated line profiles of MWC349a H26α and H30α emission. Velocity channel width is 0.53 km/s. Each point represents an individual maser spot feature we located using position centroid analysis. Color coding labels their velocity and allows for easy comparison to the plots showing maser spot position. The double peaked emission line is consistent with what is normally observed for spectral lines from a rotating body. The integrated line profiles are quite similar for the different frequency features.

This shows the flux at each frequency. In Figure 2 we have chosen to mark velocities instead of frequencies. Since the only emission we should see in this frequency band is from H26α or H30α emission we can assume that emission at any other frequency is due to a Doppler shift effect of particular maser spots. 0 velocity on each plot is the rest frequency of H26α (353 GHz) or H30α (231.9 GHz) depending on the plot. The double peaked shape is consistent with previous results indicating that the gas around MWC349a is a rotating disk.

The integrated line profile gives us very basic guesses about structure but if we want to prove any of these theories more rigorously we need a method for determining the positions of individual maser spots. For this we use Position Centroid Analysis. We take an image at a

particular frequency (one of the windows in Figure 1) and fit a 2 dimensional Gaussian intensity

model to its RA and Dec position. The location of the peak of the Gaussian in RA and Dec is

taken to be the centroid of that image and we assume that the centroid is the center of a maser

spot whose emission we are observing at that particularly frequency. Performing this procedure

on each maser spot gives us a set of positions and frequencies for each maser spot. Position

Centroid Analysis can be performed on the visibility distribution as well. When we fit our

centroid to the brightness distribution we used the MIR task imfit and when we fit our centroid to

the visibility data we use the MIR task uvfit. Generally using the visibility at provides a more

accurate fit. The results we present in this paper are all a result of working with the visibility

data.

These RA and Dec offsets give us a position for each maser spot with respect to the

center of the image. In order to calculate the error on that position we use an equation from the

discussion of position centroid analysis in Weintroub 2008:

$$\Delta\theta = \frac{1}{2} \frac{\theta_r}{S/N},$$

In this equation $\Delta\theta$ is the positional error, θr is the size of our synthesized beam, and S/N is our

signal to noise ratio. Our synthesized beam size is simply the wavelength we are observing

divided by the baseline or our interferometer. Our synthesized beam size for 353 GHz is 0.36" x

0.31" (beam is 2 dimensional). Since each frequency channel only shows the portion of the

maser emission that has that particular frequency, our signal strength varies in the different

channels. We calculated a noise value of $2.756 * 10^{-2}$ Jy/beam by measuring the standard

deviation of the intensity in a channel that did not contain any maser emission, so our noise value

is the same in each frequency channel.

For example we can calculate the positional error for our strongest feature, the channel at 31 km/s with an intensity of 98 Jy/beam, using the above equation from Weintroub 2008. Using the more conservative estimate for our synthesized beam size:

$$\Delta \theta = (1/2)(0.36") / (98/(2.758 * 10^{-2})) = 0.046 \text{ milliarcseconds}$$

This shows that for the bright maser spots we are able to achieve astoundingly high positional accuracy.

Currently we are interpreting this error as the dominant error on maser spot positions. This is a fair assumption if all our calibrations have removed all the sources of systematic error in our data. However this is an issue we still have not finished examining. As mentioned earlier, errors in the bandpass phase calibration will give erroneous positional offsets to different frequency components of the maser emission. We should examine the accuracy of our bandpass calibration and quantify its contribution to our errors for maser spot positions.

Furthermore, comparisons between the image fitting results and visibility fitting results display positional differences larger than the calculated positional error, indicating that there may be a source of systematic error we have not examined. Both the imaging and visibility data show similar overall structure, although specific maser spot positions have some small variation between the two datasets. This is another topic we should examine in the future.
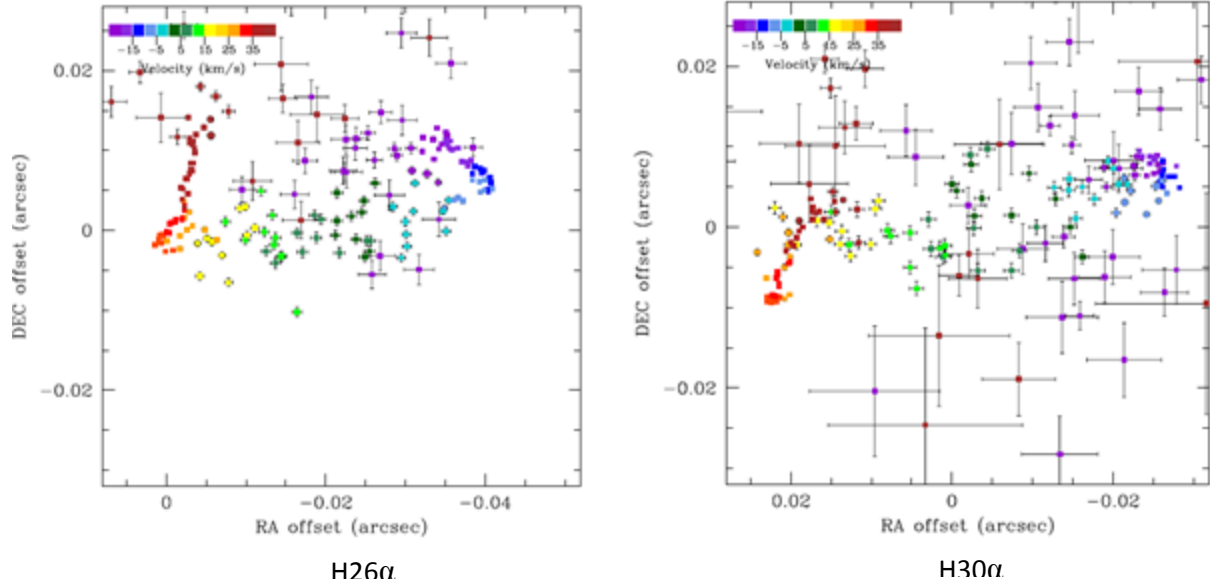
Figure 3: Plot of all maser spots and their RA and Dec uncertainties for the H26α and H30α visibility datasets. We ran uvfit on velocity channels of 0.53 km/s width from -40 km/s to 60 km/s. All spots are graphed with error bars although for many of the spots the error bars cannot be seen since they are smaller than the actual points. Note that the error bars are generally larger on the H30α maser spots than the H26α maser spots. This is because we have much stronger signal for the H26α data.

Figure 3 lends evidence to the theory of a rotating disk of gas since negative velocities are clustered on the right side of the image, positive velocities are clustered on the left side, and the lower velocity spots are spread throughout the middle of the object. However there are numerous points that have very large velocity and large error scattered around the image. One strange and unexpected result is that these high velocity features are only located above the disk for the H26α maser spots but are scattered all around the disk for the H30α maser spots. We don't have any explanation for this difference at this time but we will investigate it in future work. Most of these high error features are a result of fitting some of the weaker features towards the edge of our -40 to 60 km/s range. Figure 2 shows that these features have very low flux. This is the source of the large error on these specific features. There could be several reasons for the poor fits for these points. The first explanation is that these are simply very dim maser spots, so the signal:noise is

so low that we cannot properly perform centroid fitting. A second possibility is that there are several different discrete locations of maser emission at this velocity so the position centroid analysis is picking some average position of the various spots. Either explanation can account for the relatively random spread and high errors for these points. These high velocity features will be very important to study in the future. It is possible that some of the high velocity features are an indication of gas being ejected from the disk. (Martin-Pintado 2011) However we expect these wind features should have more reasonable errors. To decide which features are truly physical phenomenon we will need to find a method to rule out the points at which uvfit is failing to properly find the centroid of a single discrete maser spot. One strategy we employed was to make a flux cut and discard all features that had a flux less than 4 Janskys/beam in the H26α data For the sake of comparison we then discarded those same velocity features in the H30α data. This flux cut led us to discard velocity features less than -33 km/s and velocity features greater than 48.5 km/s. In total we cut 27 features from each dataset. Note that this is also similar to discarding features with high error, since our error equation incorporates signal:noise. Brighter features will have higher signal:noise and therefore lower error.
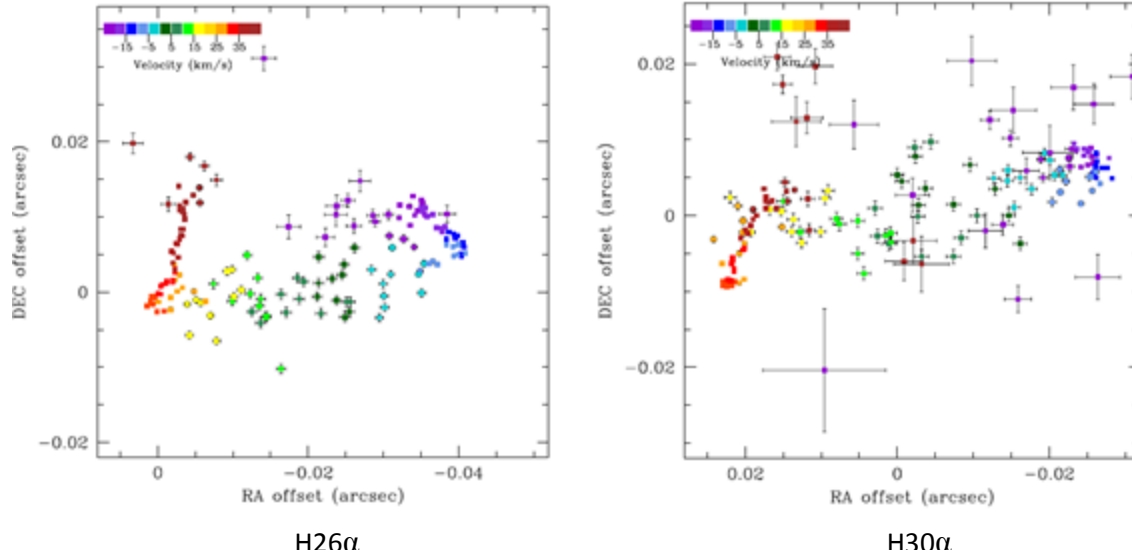
H26α   H30α

Figure 4: Plot of all H26α and H30α maser spots after the flux cut. The shape of the disk is clearly evident after the low intensity features are discarded. The left end is redshifted as it rotates towards away from us and the right end is blueshifted as it rotates towards us. Note that the center features have a velocity of ~5 km/s. This is the speed at which the entire disk is moving away from us. Note that the 0 position on the H26α dataset is lined up with the brightest emission feature at 31 km/s not the center of the disk. This is a result of the line self-calibration we performed on only the H26α dataset. The two plots can still be superimposed by merely shifting the 0 position of H26α ~0.02" to the right. The relative scale has not been affected by this positional shift.

Figure 4 allows us to see the disk shape much more clearly. There does seem to be some high velocity gas being expelled from the disk in each plot. We still are not sure whether this is the correct flux cut to make or whether another cut would be more appropriate. We have to further investigate exactly which points need to be cut and we will analyze this is future work on this data.

One interesting result is that the RA span of the H26α maser spots in the disk is slightly smaller than the RA span of the H30α maser spots in the disk. The extent of the H26α maser spots is ~0.04" while the H30α maser spots span ~0.05". This implies that H26α maser spots are forming closer to the center of the disk than the equivalent H30α spots. This is quite interesting and merits further study. One possible explanation is that the H30α masers are harder to excite

and therefore a longer column of gas is required to produce the H30α masers than the H26α

masers.
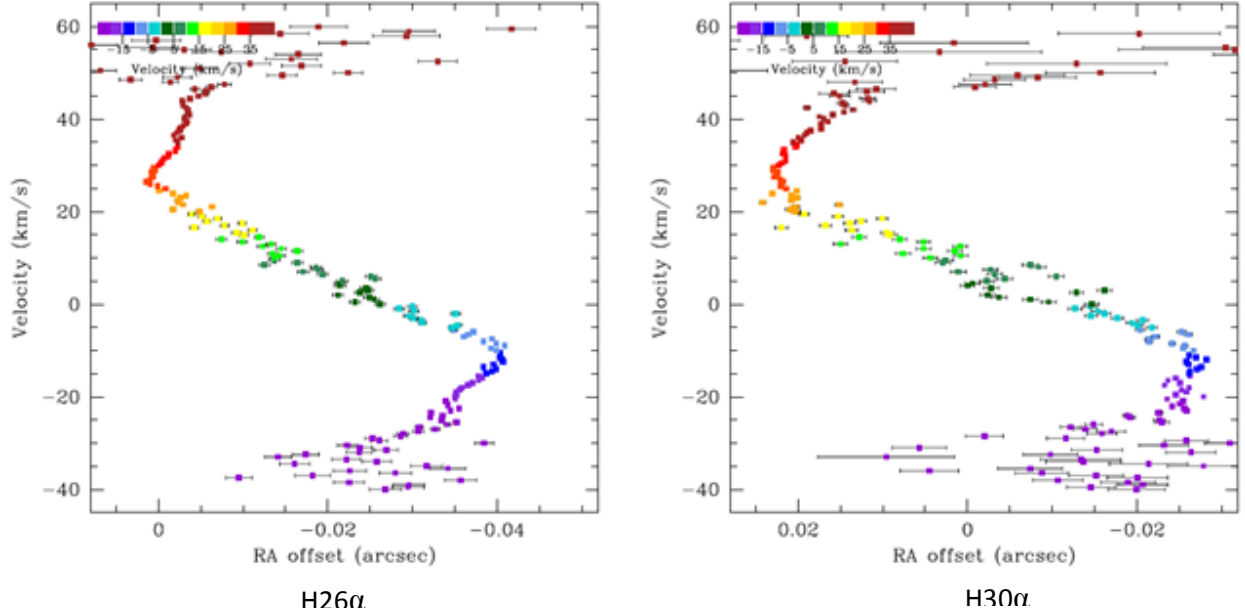
　　　　We also produced a rotation curve for each dataset.

Figure 5: Rotation curves for the H26α and H30α datasets. Note that the same RA position shift of the H26α plot is present. These rotation curves have a linear central part that corresponds to looking at the midpoint of the disk. The combination of the normal 1/r relation and a geometric projection effect of the disk makes it so the rotation curve appears linear towards the central parts of the disk. The edges of the disk (velocities ~25 to 50 and velocities ~-15 to -30) show the characteristic 1/r rotation curve although the exact form of this differs in the H26α and H30α datasets. The slope of the linear portion also differs for the different frequency maser spots.

　　　　The rotation curves are largely what we expected although the differences between the

H26α and H30α rotation curve are interesting results for us to follow up on. The rotation curve at

the edges of the disk is different for the different maser spot frequencies. Additionally the slope

of the central linear part differs between datasets; the H26α plot has a greater slope than the

H30α plot. This is consistent with our discovery that the H26α maser spots in the disk are spread

over a smaller area. Since the maser spots are distributed over a smaller area, the slope of the RA

vs. velocity plot needs to be greater to reach the same velocity features. Further analysis of these

rotation curves will be extremely useful in our attempts to map out the disk structure.

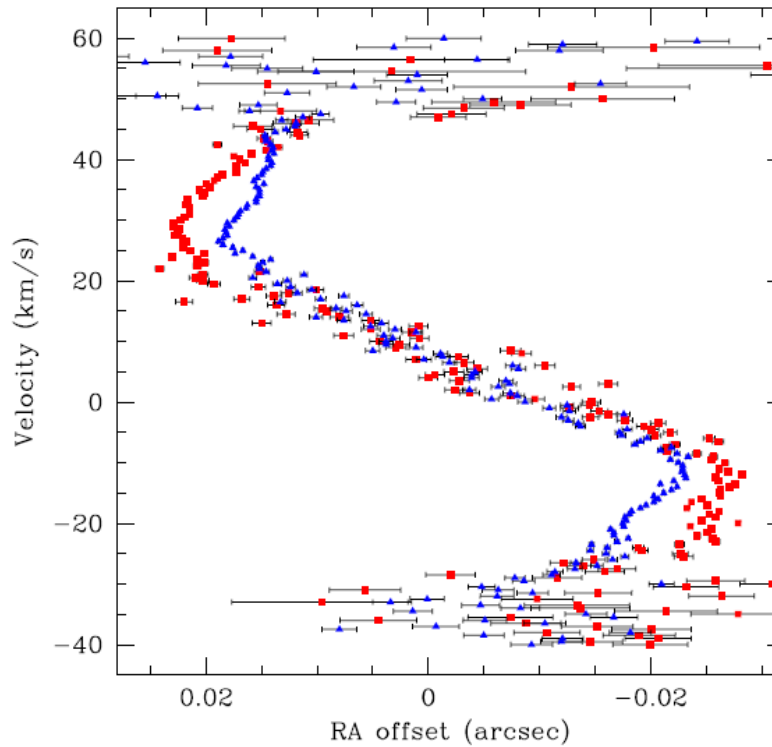In order to more easily compare the H26α and H30α rotation curves we have also produced a plot overlaying them.

Figure 6: A plot of the H26α and H30α rotation curves. The H26α points are plotted as blue triangles and the H30α points are plotted as red squares. The H26α data has been shifted by + 0.0175" RA to properly superimpose the plots.

It is obvious in the overlay plot that the linear portion of the H26α curve has a higher slope than the linear portion of the H30α curve. Also the differences between the curves at the edges of the disk become more obvious.

4. Conclusion

We have produced a map of maser spot positions with greater accuracy than any previous map. Our maser spot positions largely agree with earlier maps, such as those of Weintroub et al. 2008, but improve upon them by greatly reducing the uncertainties in maser spot position and providing a greater velocity resolution. Our strongest feature of H30α maser emission has a

positional uncertainty of 0.046 milliarcseconds: an improvement of ~40 times over Weintroub's lowest positional uncertainty of 1.8 milliarcseconds. We also have obtained the first measurements of H26α maser spot positions. Together these datasets provide an unprecedented amount of information about the maser spots around MWC349a.

In the future we will further analyze the possibility of gas being emitted from the disk. We have already discovered many high velocity features whose positions are not consistent with Keplerian motion on the disk. However, we still need to analyze which features are truly emitted gas and which are simply failures of our uvfit routine. Future work with this data should allow us to gain a greater understanding of the gas being blown off MWC349a's disk.

A lot of future work could be done using our positional data to attempt to differentiate between various structural models of the gas around MWC349a. We did not have time to study any of the particular theories of its structure but given additional time our data would be the best in the field for such an endeavor. Using both H26α and H30α maser spot positional data should give us many opportunities to refine models of this disk.

Our positional accuracy could still be improved upon. The weather was not optimal during our observation period so even another project using the SMA in an identical configuration would have a chance of improving upon our uncertainties if the weather is better and allows them to get a better signal to noise ratio. More promising would be to carry out this experiment on an interferometer with even longer baselines. Then even sub optimal weather conditions and an equivalent signal to noise ratio would result in great improvements over our positional accuracy measurements.